Published in "Science 332(6032): 937-940, 2011"
which should be cited to refer to this work.

Dimensionality Control of Electronic Phase Transitions in Nickel-Oxide Superlattices

A. V. Boris,[1]* Y. Matiks,[1] E. Benckiser,[1] A. Frano,[1] P. Popovich,[1] V. Hinkov,[1] P. Wochner,[2] M. Castro-Colin,[2] E. Detemple,[2] V. K. Malik,[3] C. Bernhard,[3] T. Prokscha,[4] A. Suter,[4] Z. Salman,[4] E. Morenzoni,[4] G. Cristiani,[1] H.-U. Habermeier,[1] B. Keimer[1]*

The competition between collective quantum phases in materials with strongly correlated electrons depends sensitively on the dimensionality of the electron system, which is difficult to control by standard solid-state chemistry. We have fabricated superlattices of the paramagnetic metal lanthanum nickelate ($LaNiO_3$) and the wide-gap insulator lanthanum aluminate ($LaAlO_3$) with atomically precise layer sequences. We used optical ellipsometry and low-energy muon spin rotation to show that superlattices with $LaNiO_3$ as thin as two unit cells undergo a sequence of collective metal-insulator and antiferromagnetic transitions as a function of decreasing temperature, whereas samples with thicker $LaNiO_3$ layers remain metallic and paramagnetic at all temperatures. Metal-oxide superlattices thus allow control of the dimensionality and collective phase behavior of correlated-electron systems.

Since the discovery of high-temperature superconductivity two decades ago, much effort has been undertaken to explore and understand the quantum physics of strongly correlated electrons in transition metal oxides (TMOs) (*1*). The electronic phases can exhibit radically different physical properties, and a new generation of electronic devices will become possible if the competition between these phases can be systematically controlled (*2*). However, the control options offered by conventional solid-state chemistry are limited. The charge carrier concentration in a TMO compound, for instance, can be modified by chemical substitution (*3*), but only at the expense of altering the local lattice structure and electronic energy levels in an uncontrolled manner. The dimensionality of the electron system, D, is another key control parameter, because low-dimensional metals are known to be more susceptible to collective ordering phenomena (including spin- and charge-ordering instabilities, as well as unconventional superconductivity) than their higher-dimensional counterparts. Some level of dimensionality control has been achieved by synthesizing compounds in the Ruddlesden-Popper series of perovskite structures, which comprise N consecutive TMO layers per unit cell. In principle, the dimensionality of the electron system in these materials can thus be tuned from $D = 2$ to 3 by increasing N. In practice, however, the synthesis requirements become rapidly more demanding for large N, and many Ruddlesden-Popper phases have turned out to be unstable.

Recent advances in the synthesis of TMO heterostructures with atomically sharp interfaces indicate an alternative route toward control of correlated-electron systems (*2*). In principle, the carrier concentration in a heterostructure can be tuned by a gate voltage in a field-effect arrangement, without introducing substitutional disorder, and the dimensionality can be modified by means of the deposition sequence of electronically active and inactive TMO layers. In practice, however, attempts to implement this approach have faced many of the same difficulties encountered in the chemical synthesis of bulk materials. For instance, defects created by interdiffusion or strain relaxation can influence the transport properties of the interfacial electron system in an uncontrolled manner. These difficulties are compounded by the paucity of experimental methods capable of probing the collective phase behavior of electrons in TMO heterostructures. Whereas ferromagnetism and ferroelectricity can be detected on the basis of the macroscopic magnetic- or electric-field distribution, the identification of two of the most common collective ordering phenomena of correlated electrons—namely, charge order and antiferromagnetism—in TMO heterostructures and superlattices is much more difficult.

Motivated by the desire to overcome these difficulties and to realize the potential of TMO heterostructures in controlling collective quantum phases, we have carried out a comprehensive experimental study of superlattices based on the correlated metal $LaNiO_3$, in which the dimensionality of the electron system was used as a control parameter, but the influence of epitaxial strain and defects was carefully monitored. An extensive body of earlier work on bulk nickelates provides an excellent background for our study. Whereas bulk $LaNiO_3$ is a three-dimensional (3D) Fermi liquid (*4*) that remains paramagnetic

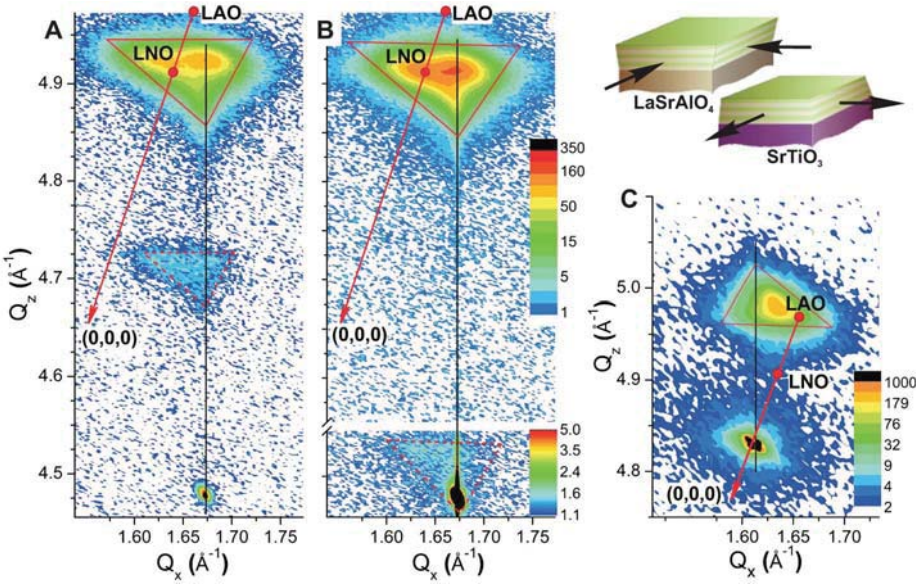

Fig. 1. Reciprocal-space maps of 100-nm-thick $LaNiO_3$ [N unit cells (u.c.)]/$LaAlO_3$ (N u.c.) superlattices grown under compressive strain on $LaSrAlO_4$ (001) with (**A**) $N = 4$, (**B**) $N = 2$, and (**C**) under tensile strain on $SrTiO_3$ (001) with $N = 2$. The black vertical lines indicate the in-plane (Q_x) position of the $LaSrAlO_4$ (109) and $SrTiO_3$ (103) reflections. The strain state of the perovskite epilayers is identified by the intensity distribution in the vicinity of the (103) layer Bragg peak and its superlattice satellite, which are delineated by solid- and dashed-line triangles, respectively. The reciprocal spacings of 103 strain-free pseudocubic $LaNiO_3$ (LNO) and $LaAlO_3$ (LAO) are indicated by the red circles. The red arrows point toward the origin.

[1]Max-Planck-Institut für Festkörperforschung, Heisenbergstrasse 1, D-70569 Stuttgart, Germany. [2]Max-Planck-Institut für Metallforschung, Heisenbergstrasse 3, D-70569 Stuttgart, Germany. [3]Department of Physics, University of Fribourg and Fribourg Center for Nano Materials, CH-1700 Fribourg, Switzerland. [4]Laboratory for Muon Spin Spectroscopy, Paul Scherrer Institute (PSI), CH-5232 Villigen PSI, Switzerland.

*To whom correspondence should be addressed. E-mail: A.Boris@fkf.mpg.de (A.V.B.); B.Keimer@fkf.mpg.de (B.K.)

and metallic at all temperatures, other lanthanide nickelates ($RNiO_3$) with smaller electronic bandwidths exhibit collective metal-insulator transitions with decreasing temperature (*3*). In the insulating low-temperature phase, they exhibit a periodic superstructure of the valence-electron charge and a noncollinear antiferromagnetic ordering pattern of spins on the Ni atoms (*5*–*8*). This implies that the itinerant conduction electrons of $LaNiO_3$ are highly correlated and on the verge of localization. Experiments on a controlled number of atomically thin $LaNiO_3$ layers separated by the electronically inactive wide-gap insulator $LaAlO_3$ are thus well suited for attempts to control the phase behavior of a correlated-electron system via its dimensionality. We have used wide-band spectroscopic ellipsometry to accurately determine the dynamical electrical conductivity and permittivity, which (in contrast to the dc conductivity) are not influenced by misfit dislocations. Low-energy muons, which are stopped in the superlattice (SL) before they reach the substrate, served as a sensitive probe of the internal magnetic field distribution. Two consecutive, sharp phase transitions in the charge and spin sector revealed by this experimental approach demonstrate that the electronic properties of our SLs are determined by electron correlations and not by interfacial disorder. By changing the $LaNiO_3$ layer thickness, we demonstrate full dimensionality control over the collective phase behavior.

The SLs were grown by pulsed-laser deposition (*9*, *10*) and comprised N consecutive layers of $LaNiO_3$ and the $LaAlO_3$. To discriminate between the influence of dimensionality and epitaxial strain, we have grown SLs on both $SrTiO_3$, which induces tensile strain in the overlayer, and $LaSrAlO_4$, which induces compressive strain. Figure 1 shows contour maps of the diffracted x-ray intensity distribution in the vicinity of the 103 perovskite Bragg peak for three representative samples: $N = 4$ and $N = 2$ SLs grown on $LaSrAlO_4$ (001) and an $N = 2$ SL on $SrTiO_3$ (001). Both the position and shape of the overlayer reflection are strongly affected by inversion of the type of substrate-induced strain (Fig. 1, B and C), but they remain essentially unchanged by varying the individual layer thicknesses N (Fig. 1, A and B). A detailed analysis of the substrate-induced strain and relaxation effects is provided in the Supporting Online Material (SOM) (*10*). In the following text, we show that the transport and magnetic properties of the SLs are only weakly influenced by the strain-induced local structural distortions and interfacial defects, but they are qualitatively transformed by varying the number of consecutive unit cells within the $LaNiO_3$ layers.

The charge transport properties of the SLs were determined by spectral ellipsometry, which yields the frequency-dependent complex dielectric function $\varepsilon(\omega) = \varepsilon_1(\omega) + i\varepsilon_2(\omega)$, related to the optical conductivity $\sigma(\omega)$ by $\varepsilon(\omega) = 1 + 4\pi i\sigma(\omega)/\omega$. This method is very sensitive to thin-film properties because of the oblique incidence of light, and it is insensitive to the influence of strain-induced extended defects on the current flow through the atomically thin layers (*10*, *11*). Figure 2, A and B, shows the infrared spectra of $\varepsilon_2(\omega)$ for $N = 4$ and 2 SLs grown on $LaSrAlO_4$ and $SrTiO_3$, respectively, which are representative of the in-plane dielectric response of the metallic $LaNiO_3$ layers. The insets show the corresponding temperature dependencies of ε_2 at a fixed photon energy $\hbar\omega = 30$ meV ($\hbar$, Planck's constant h divided by 2π). The gradual evolution of ε_2 with temperature over the far-infrared range confirms that the $N = 4$ SLs remain metallic at all temperatures. The $N = 2$ SLs, on the other hand, show clear evidence of a metal-insulator (MI) transition upon cooling, with a sharp onset at the transition temperatures $T_{MI} = 150$ and 100 K for SLs grown on $LaSrAlO_4$ and $SrTiO_3$, respectively. For $T \gtrsim T_{MI}$, the infrared $\varepsilon(\omega)$ spectrum of $N = 2$ SL is well described by a broad Drude response $\varepsilon(\omega) = \varepsilon_\infty - \omega_{pl}^2/(\omega^2 + i\omega\gamma)$ with a ratio of scattering rate and plasma frequency $\gamma/\omega_{pl} \approx 0.2$ (lower shaded line in Fig. 2A) that is typical for bulk complex oxides. The effective mass enhancement m^*/m is estimated from the plasma frequency as $m^*/m = \frac{4\pi n_{Ni}}{m\omega_{pl}^2}$, where $n_{Ni} = \frac{1}{2} \times 1.7 \times 10^{22}$ cm^{-3}, by assuming one electron per Ni atom. With $\omega_{pl} \approx 1.1$ eV [Fig. 2A and fig. S7

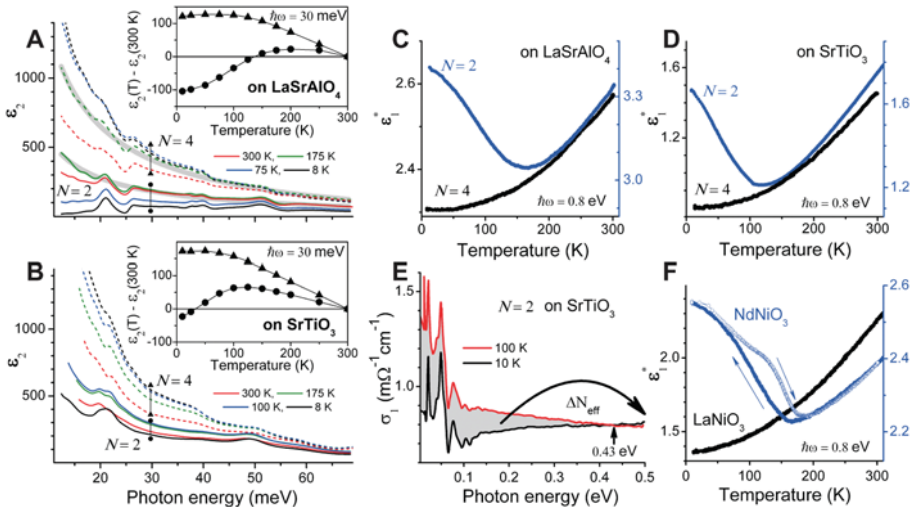

Fig. 2. (**A** and **B**) $\varepsilon_2(\omega)$ spectra of the $N = 2$ (solid lines, circles) and $N = 4$ (dashed lines, triangles) SLs on (A) $LaSrAlO_4$ and (B) $SrTiO_3$ substrates measured at representative temperatures. The shaded lines in (A) represent the Drude model fit to $\varepsilon_2(\omega)$ at 175 K for the $N = 2$ ($N = 4$) SL with $\omega_{pl} = 1.05$ eV (1.10 eV) and $\gamma = 200$ meV (90 meV). The insets provide the corresponding temperature dependencies of ε_2 at a photon energy of $\hbar\omega = 30$ meV for the $N = 2$ (circles) and $N = 4$ (triangles) SLs. (**C** and **D**) Temperature dependence of the as-measured pseudodielectric permittivity ε_1^* at $\hbar\omega = 0.8$ eV in the $N = 2$ (blue) and $N = 4$ (black) SLs on (C) $LaSrAlO_4$ and (D) $SrTiO_3$. (**E**) The difference between the optical conductivity spectra $\sigma_1(100\text{ K}, \omega)$ and $\sigma_1(10\text{ K}, \omega)$ (shaded area) quantifies the reduction of the effective charge density, $\Delta SW \approx 0.03$ per Ni atom, within the gap energy range below 0.43 eV at the charge ordering transition in the $N = 2$ superlattice on $SrTiO_3$. (**F**) Temperature dependence of ε_1^* at 0.8 eV of reference 100-nm films of $LaNiO_3$ (black) and $NdNiO_3$ (blue).

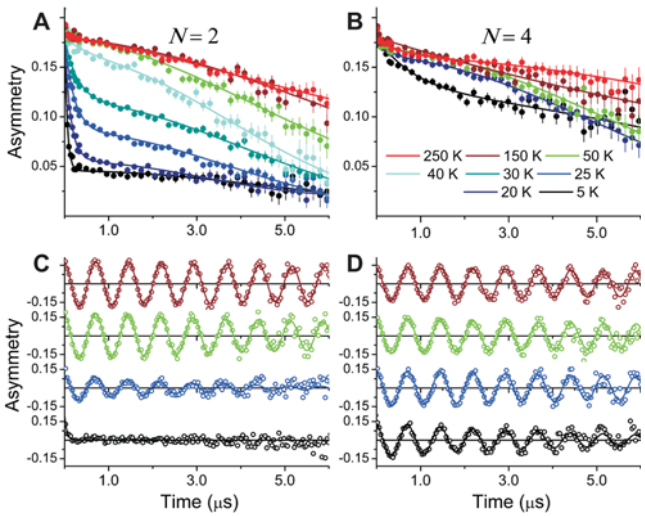

Fig. 3. Time evolution of the zero-field muon spin polarization at various temperatures for the (**A**) $N = 2$ and (**B**) $N = 4$ superlattice on $LaSrAlO_4$. (**C** and **D**) Muon spin relaxation spectra in a weak transverse magnetic field of 100 G in the superlattices as in (A) and (B), respectively. (A) to (D) use the color coding in the legend shown in (B).

in the SOM (*10*)], we obtain $m^*/m \approx 10$, which is in good agreement with the value for bulk $LaNiO_3$ obtained from specific heat measurements (*12*). Using the Fermi energy $E_F = 0.5$ eV derived from the thermopower of $LaNiO_3$ (*12*) and γ from the Drude model fit to the infrared spectra, we estimate the mean free path as $l = \frac{1}{2\pi c\gamma}\sqrt{2E_F/m*}$ (c, speed of light). For the $N = 2$ and $N = 4$ SLs on both substrates, we obtain $l = 5$ to 6 Å and 10 to 12 Å, respectively (*10*). Remarkably, the mean free path correlates with the individual $LaNiO_3$ layer thickness, testifying to the high quality of the interfaces.

The charge-carrier localization at lower temperature can be readily identified through a rapid drop in $\varepsilon_2(T)$ and progressive deviation of $\varepsilon_2(\omega)$ from the Drude function due to the formation of a charge gap. The temperature evolution of the real part of the dielectric function provides complementary information about the optical spectral-weight redistribution at T_{MI}. Figure 2, C and D, show the temperature dependence of the as-measured permittivity, ε_1^*, at an energy above the gap ($\hbar\omega$ = 0.8 eV). In the metallic phase, ε_1^* decreases with decreasing temperature, following the temperature dependence of the scattering rate $\gamma(T)$. This is characteristic of a narrowing of the Drude peak where the spectral weight is removed from the high-energy tail and transferred to the far-infrared range near the origin. The charge-gap formation below T_{MI} in $N = 2$ SLs leads to the reverse spectral-weight transfer from the inner-gap region to excitations across the gap and, as a consequence, to an increase in ε_1^*.

The consistent temperature evolution of ε_1 and ε_2 over a broad range of photon energies demonstrates the intrinsic nature of the charge-localization transition observed in SLs with $N = 2$ and provides clues to its origin. The spectral-weight reduction within the gap can be quantified in terms of the effective number of charge carriers per Ni atom and extracted from a sum-rule analysis as $\Delta SW = \frac{2m}{\pi e^2 n_{Ni}}\int_0^{\Omega_G}[\sigma_1(T \approx T_{MI},\omega) - \sigma_1(T << T_{MI},\omega)]d\omega$, where m is the free-electron mass, e is the charge on the electron, and n_{Ni} is the density of Ni atoms. The upper integration limit, $\Omega_G \approx 0.43$ eV, is a measure of the charge gap and can be identified with the equal-absorption (or isosbestic) point, where $\sigma_1(\omega)$ curves at different temperatures intersect (Fig. 2E). The charge-gap formation on this energy scale can be attributed to a charge-ordering instability, as in the case of bulk lanthanide nickelates ($RNiO_3$) with smaller R-ion radius (*5*–*8*). The spectral weight $\Delta SW \approx 0.03$ below $\Omega_G \approx 0.43$ eV determined for the $N = 2$ SLs (Fig. 2E) is of the same order as, albeit somewhat lower than, the corresponding quantity $\Delta SW = 0.058$ below $\Omega_G \approx 0.3$ eV reported at the metal-insulator transition in bulk $NdNiO_3$, which is known to be due to charge order (*13*). To highlight the analogy to the behavior in bulk nickelates, Fig. 2F shows reference measurements on single 100-nm-thick films of $NdNiO_3$ and $LaNiO_3$, measured under the same conditions as in Figs. 2, C and D. Because ε_1^* at 0.8 eV for the single $NdNiO_3$ film displays closely similar temperature dependence as found for $N = 2$ SLs, we conclude that the gap formation in the latter case also reflects charge ordering. In $NdNiO_3$, the metal-insulator transition occurs as a first-order transition with a concomitant noncollinear antiferromagnetic ordering at the Néel temperature $T_N = T_{MI}$ (*6*–*8*). The thermal hysteresis in the $\varepsilon_1^*(T)$ curve in Fig. 2F is consistent with the first-order character of the transition, with uniform and charge-ordered phases coexisting over a broad temperature range. In contrast, there is no discernible hysteresis observed in $\varepsilon_1^*(T)$ of $N = 2$ SLs (Fig. 2, C and D), which suggests a second-order transition. Continuing the analogy with the bulk nickelate series, one would then expect another second-order transition due to the onset of antiferromagnetic ordering at $T_N < T_{MI}$ in the $N = 2$ SLs, as in $RNiO_3$ with small R (Lu through Sm).

To test this hypothesis, we carried out low-energy muon spin rotation (μSR) measurements using the μE4 beamline at the Paul Scherrer Institute (*10*, *14*), where positive muons with extremely reduced velocity can be implanted into specimens and brought to rest between the substrate and the $LaAlO_3$ capping layer. Because the muons decay into positrons preferentially along the spin direction, they act as highly sensitive local magnetic probes. Figure 3A shows muon decay asymmetry data from a SL with $N = 2$ at selected temperatures with no external field. At $T > 50$ K, the asymmetry is described by a Gaussian with relatively slow relaxation, σ, given by $A(0) \times \exp(-\sigma^2 t^2/2)$, where t is time (solid lines in Fig. 3A), typical of dipolar magnetic fields generated by nuclear moments of La and Al. As the temperature decreases, there is a gradual increase in σ from 0.17 μs^{-1} at 250 K to 0.27 μs^{-1} at 20 K. Below 50 K the asymmetry drops sharply, and the μSR spectra can be fitted well by introducing an additional exponential relaxation $\exp(-\Lambda t)$. The fast depolarization rate Λ reaches a value of ≈17 μs^{-1} at 5 K, implying a resulting Lorentzian distribution of local fields with half width at half maximum $\Delta B = 0.75\Lambda/\gamma_\mu \approx 150$ G, where $\gamma_\mu = 2\pi \times 13.55$ MHz/kG is the muon's gyromagnetic ratio (*10*). The fast increase in Λ with decreasing temperature below 50 K is similar to the behavior in bulk $NdNiO_3$ (*15*) and $(Y,Lu)NiO_3$ (*16*) below T_N, caused by static internal fields from ordered Ni magnetic moments. The wide field distribution ΔB and the absence of a unique muon precession frequency reflects the SL structure with several inequivalent muon stopping sites in the alternating magnetic ($LaNiO_3$) and nonmagnetic ($LaAlO_3$) layers, probably compounded by a complex noncollinear spin structure as in the bulk nickelates (*15*, *16*).

We used 100-G transverse field (TF) measurements to determine the fraction of muons, f_m, experiencing static local magnetic fields $B_{loc} > B_{TF}$ (i.e., showing no detectable precession with $\omega = \gamma_\mu B_{TF}$) (*10*). Figure 3C indicates that the $N = 2$ SL shows a transition from an entirely paramagnetic muon environment ($f_m = 0$) to a nearly full volume of static internal fields, with a sharp onset at $T_N \sim 50$ K. The magnetic state at 5 K is robust against externally applied transverse fields up to 3 kG (not shown in Fig. 3), which is the limit of time resolution of our setup. The continuous temperature dependence of f_m (Fig. 4) and the absence of thermal hysteresis indicate that the magnetic transition for the $N = 2$ SLs is second-order. At the same time, Fig. 3, B and D, show that SLs with thicker $LaNiO_3$ layers remain paramagnetic down to the lowest temperatures, as in bulk $LaNiO_3$. An additional slow exponential relaxation with $\Lambda = 0.9$ μs^{-1} is seen only at $T = 5$ K (black symbols and curve in Fig. 3B). This results in a small increase in relaxation rate, but no loss in asymmetry of the TF μSR signal (Fig. 3D). The effect is probably due to weak dynamical spin correlations that are quenched already in a field of 100 G, in clear contrast to the long-range static magnetic order observed in the $N = 2$ samples.

As a local probe, μSR does not allow definite conclusions about the magnetic ordering pattern in the $N = 2$ SLs. However, we can rule out ferromagnetism on the basis of an estimate of the ordered moment, μ_{Ni}, on the Ni sites from the distribution of local fields experienced by the muons. The highest local field at the shortest μ-Ni distance, $c/4$ (where c is the lattice parameter of the orthorhombic unit cell) ≈ 1.92 Å (*15*), is 4 to 5 times ΔB, which corresponds to $\mu_{Ni} \gtrsim 0.5\mu_B$. If these moments were co-aligned in the ordered state, the corresponding total moment $M = \mu_{Ni} n_{Ni} V_{SL} \gtrsim 7.7 \times 10^{-4}$ emu (where V_{SL} is the volume of the superlattice) would have been readily detected in magnetization measurements. The absence of such an effect is confirmed in magnetometric measurements with sensitivity $\sim 10^{-7}$ emu.

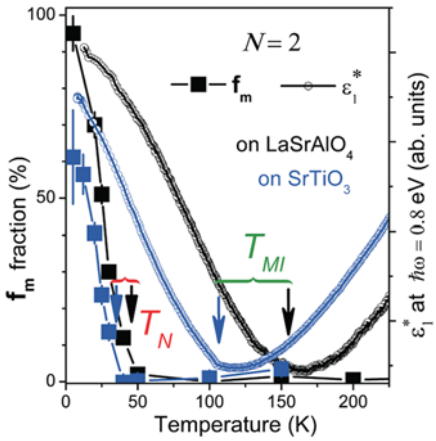

Fig. 4. Temperature dependencies of the fraction of muons experiencing static local magnetic fields, f_m, and the normalized permittivity ε_1^* at 0.8 eV (in arbitrary units) in the $N = 2$ superlattices. The black and blue arrows mark the magnetic (T_N) and metal-insulator (T_{MI}) transition temperatures for the superlattices on $LaSrAlO_4$ and $SrTiO_3$, respectively.

Figure 4 summarizes the phase behavior of the SLs with $N = 2$, which undergo a sequence of two sharp, collective electronic phase transitions upon cooling. We have provided strong evidence that the two transitions correspond to the onset of charge and spin order. By showing that the $N = 4$ counterparts remain uniformly metallic and paramagnetic at all temperatures, we have demonstrated full dimensionality control of these collective instabilities. The higher propensity toward charge and spin order in the 2D systems probably reflects enhanced nesting of the $LaNiO_3$ Fermi surface. The phase behavior is qualitatively similar to the one observed in bulk $RNiO_3$ with small radius of the R anions, which results from bandwidth narrowing due to rotation of NiO_6 octahedra, but the transition temperatures and the order parameters are substantially lower, probably because of the reduced dimensionality. Because the transitions occur in the $N = 2$ SLs, regardless of whether the substrate-induced strain is compressive (Fig. 1B) or tensile (Fig. 1C), structural parameters such as rotation and elongation of the NiO_6 octahedra can be ruled out as primary driving forces. We note, however, that the infrared conductivity is higher (Fig. 2, A and B) and the transition temperatures are lower (Fig. 4) in the $N = 2$ SL grown under tensile strain. The more metallic response of these SLs, compared with those grown under compressive strain, may reflect a widening of the Ni 3d-electron bandwidth and/or an enhanced occupation of the Ni $d_{x^2-y^2}$ orbital polarized parallel to the $LaNiO_3$ layers. A small orbital polarization was indeed detected by soft x-ray reflectometry in our superlattices (*17*). This indicates further opportunities for orbital control of the collective phase behavior of the nickelates, which may enable experimental tests of theories predicting high-temperature superconductivity (*18*, *19*) or multiferroicity (*20*) in these systems.

References and Notes

1. E. Dagotto, *Science* **309**, 257 (2005).
2. J. Mannhart, D. G. Schlom, *Science* **327**, 1607 (2010).
3. M. Imada, A. Fujimori, Y. Tokura, *Rev. Mod. Phys.* **70**, 1039 (1998).
4. R. Eguchi *et al*., *Phys. Rev. B* **79**, 115122 (2009).
5. I. I. Mazin *et al*., *Phys. Rev. Lett.* **98**, 176406 (2007).
6. J. L. García-Muñoz, M. A. G. Aranda, J. A. Alonso, M. J. Martínez-Lope, *Phys. Rev. B* **79**, 134432 (2009).
7. V. Scagnoli *et al*., *Phys. Rev. B* **73**, 100409(R) (2006).
8. V. Scagnoli *et al*., *Phys. Rev. B* **77**, 115138 (2008).
9. H.-U. Habermeier, *Mater. Today* **10**, 34 (2007).
10. Materials and methods are available as supporting materials on *Science* Online.
11. J. W. Freeland *et al*., *Phys. Rev. B* **81**, 094414 (2010).
12. X. Q. Xu, J. L. Peng, Z. Y. Li, H. L. Ju, R. L. Greene, *Phys. Rev. B* **48**, 1112 (1993).
13. T. Katsufuji, Y. Okimoto, T. Arima, Y. Tokura, J. B. Torrance, *Phys. Rev. B* **51**, 4830 (1995).
14. T. Prokscha *et al*., *Nucl. Instrum. Methods Phys. Res. A* **595**, 317 (2008).
15. J. L. García-Muñoz, P. Lacorre, R. Cywinski, *Phys. Rev. B* **51**, 15197 (1995).
16. J. L. García-Muñoz *et al*., *Physica B* **374–375**, 87 (2006).
17. E. Benckiser *et al*., *Nat. Mater.* **10**, 189 (2011).
18. J. Chaloupka, G. Khaliullin, *Phys. Rev. Lett.* **100**, 016404 (2008).
19. P. Hansmann *et al*., *Phys. Rev. Lett.* **103**, 016401 (2009).
20. G. Giovannetti, S. Kumar, D. Khomskii, S. Picozzi, J. van den Brink, *Phys. Rev. Lett.* **103**, 156401 (2009).

Acknowledgments: We thank Y.-L. Mathis and R. Weigel for support at the infrared IR1 and Max-Planck-Institut für Metallforschung x-ray beamlines of the synchrotron facility Angström Quelle Karlsruhe (ANKA) at the Karlsruhe Institute of Technology. We thank G. Khaliullin and O. K. Andersen for discussions, W. Sigle and P. A. van Aken for support and discussions of transmission EM results, A. Szökefalvi-Nagy for x-ray software support, and G. Logvenov for support in sample growth and characterization. This work was supported by the Deutsche Forschungsgemeinschaft, grant TRR80, project C1. V.K.M. and C.B. were supported by the Schweizerische Nationalfonds via grants 200020-129484 and NCCR-MaNEP.

Supporting Online Material

Materials and Methods
Figs. S1 to S10
Table S1
References